Acta Biomaterialia xxx (2014) xxx–xxx

Contents lists available at ScienceDirect

Acta Biomaterialia

journal homepage: www.elsevier.com/locate/actabiomat

A spider's biological vibration filter: Micromechanical characteristics of a biomaterial surface

Seth L. Young [a], Marius Chyasnavichyus [a], Maxim Erko [b], Friedrich G. Barth [c], Peter Fratzl [b], Igor Zlotnikov [b], Yael Politi [b], Vladimir V. Tsukruk [a,*]

[a] School of Materials Science and Engineering, Georgia Institute of Technology, Atlanta, GA 30332, USA
[b] Department of Biomaterials, Max Planck Institute of Colloids and Interfaces, Research Campus Golm, 14424 Potsdam, Germany
[c] Department of Neurobiology, University of Vienna, 1090 Vienna, Austria

ARTICLE INFO

Article history:
Received 10 April 2014
Received in revised form 17 July 2014
Accepted 20 July 2014
Available online xxxx

Keywords:
Biomechanics
Viscoelasticity
Atomic force spectroscopy
Biosensor materials
Stimulus transmission

ABSTRACT

A strain-sensing lyriform organ (HS-10) found on all of the legs of a Central American wandering spider (*Cupiennius salei*) detects courtship, prey and predator vibrations transmitted by the plant on which it sits. It has been suggested that the viscoelastic properties of a cuticular pad directly adjacent to the sensory organ contribute to the organ's pronounced high-pass characteristics. Here, we investigate the micromechanical properties of the cuticular pad biomaterial in search of a deeper understanding of its impact on the function of the vibration sensor. These properties are considered to be an effective adaptation for the selective detection of signals for frequencies >40 Hz. Using surface force spectroscopy mapping we determine the elastic modulus of the pad surface over a temperature range of 15–40 °C at various loading frequencies. In the glassy state, the elastic modulus was ~100 MPa, while in the rubbery state the elastic modulus decreased to 20 MPa. These data are analyzed according to the principle of time–temperature superposition to construct a master curve that relates mechanical properties, temperature and stimulus frequencies. By estimating the loss and storage moduli vs. temperature and frequency it was possible to make a direct comparison with electrophysiology experiments, and it was found that the dissipation of energy occurs within a frequency window whose position is controlled by environmental temperatures.

1. Introduction

Biological sensory organs are indispensable for an organism to receive, interpret and respond to environmental stimuli, and serve as a popular source of inspiration for biomimetic engineering [1–8]. Spiders possess remarkably well-developed mechanosensory systems and rely heavily on their ability to detect biologically relevant vibratory signals when hunting and courting [9–15]. In the highlands of Central America [8,15] the nocturnal wandering spider *Cupiennius salei* sits on mechanically stiff plants (e.g., on a banana plant or a bromeliad) which transmit substrate vibrations caused by nearby prey, predators or potential sexual partners surprisingly well (Fig. 1) [4,16]. The sense organ responsible for the spider's highly developed vibration sensitivity is composed of 21 strain-sensitive innervated slits embedded in the cuticular exoskeleton [6,17]. Because of the similarity in their appearance to the ancient musical instrument, such organs are referred to as lyriform organs [6,9,18]. Such lyriform organs are very common and can be found in many species of spiders, and well as many other arachnids, such as scorpions [6].

The vibration-sensitive lyriform organ is found at the distal end of the metatarsus (the second-last segment of the leg) in the middle of its dorsal surface on each leg (see Fig. 2B) [6,12,17]. The slits of the metatarsal lyriform organ are oriented perpendicular to the long axis of the leg, bridging a deep furrow in the metatarsus (Fig. 2C), which increases the mechanical compliance at the site of the organ and thus its sensitivity to strains in the exoskeleton [6]. Strains due to external mechanical stimuli occur as the tarsus, resting on the plant, is deflected upwards and presses against the metatarsus as a result of substrate vibrations, ultimately compressing the slits [6,9,12,19].

Along with its extreme sensitivity to substrate vibrations, the metatarsal lyriform organ is also known to effectively filter out low-frequency background noise, an ever-present problem in sensory biology [6,7]. Electrophysiological experiments on *C. salei* generated tuning (threshold) curves of the organ's slits which demonstrate their high-pass properties [9]. The threshold deflections of

* Corresponding author. Tel.: +1 404 894 6081; fax: +1 404 385 3112.
E-mail address: vladimir@mse.gatech.edu (V.V. Tsukruk).

http://dx.doi.org/10.1016/j.actbio.2014.07.023
1742-7061/

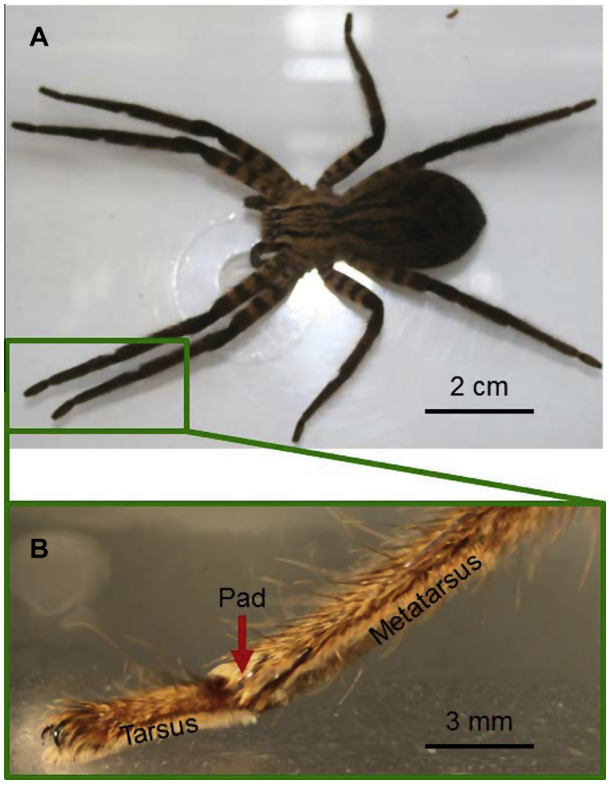

Fig. 1. (A) Adult female *Cupiennius salei*. (B) The distal end of a leg of *Cupiennius* with an arrow pointing to the joint between tarsus and metatarsus.

the tarsus required to elicit a nervous response from the sensory cells innervating the slits are of the order of 10^{-5}–10^{-4} m for vibration frequencies ranging between 0.1 and ~40 Hz, while deflections as small as 10^{-9}–10^{-8} m are sufficient to elicit action potentials for frequencies >40 Hz [6,9,19].

The processing of environmental stimuli, however, is not a function of sensory cells and the central nervous system alone. Rather, the pre-filtering of external stimuli for the fine-tuning of sensory systems is also a function of the morphology and materials properties of both the organs themselves and the cuticle in which they are embedded [7,20]. In fact, McConney et al. [12] found that one mechanism responsible for the high-pass behavior of the metatarsal vibration receptor is the viscoelastic, time-dependent behavior of the cuticular pad adjacent to the organ which transmits the stimulus from the tarsus to the metatarsus with dramatic changes in mechanical properties depending on frequency and temperature.

As is well known, viscoelastic materials display pronounced time- and temperature-dependent mechanical properties [21–25]. McConney et al. [12] used atomic force microscopy (AFM) to determine the pad's elastic modulus at its surface as a function of probing rate. They found a sharp increase in the elastic modulus from ~10–20 MPa at probing rates ranging from 0.1 to 10 Hz to >70 MPa at probing rates above 30 Hz. This finding mirrors the electrophysiologically determined tuning curves [6,9] with remarakable fidelity. By applying the principle of time-temperature superposition and by using the Williams–Landel–Ferry (WLF) equation [23], the glass transition temperature was estimated to be 25 ± 2 °C [12]. A deeper understanding of the role which viscoelasticity plays for stimulus transmission in mechanosensory organs requires direct measurements. This will also establish a basis for the design of highly selective and specific, biologically inspired synthetic sensing systems [7,26,27].

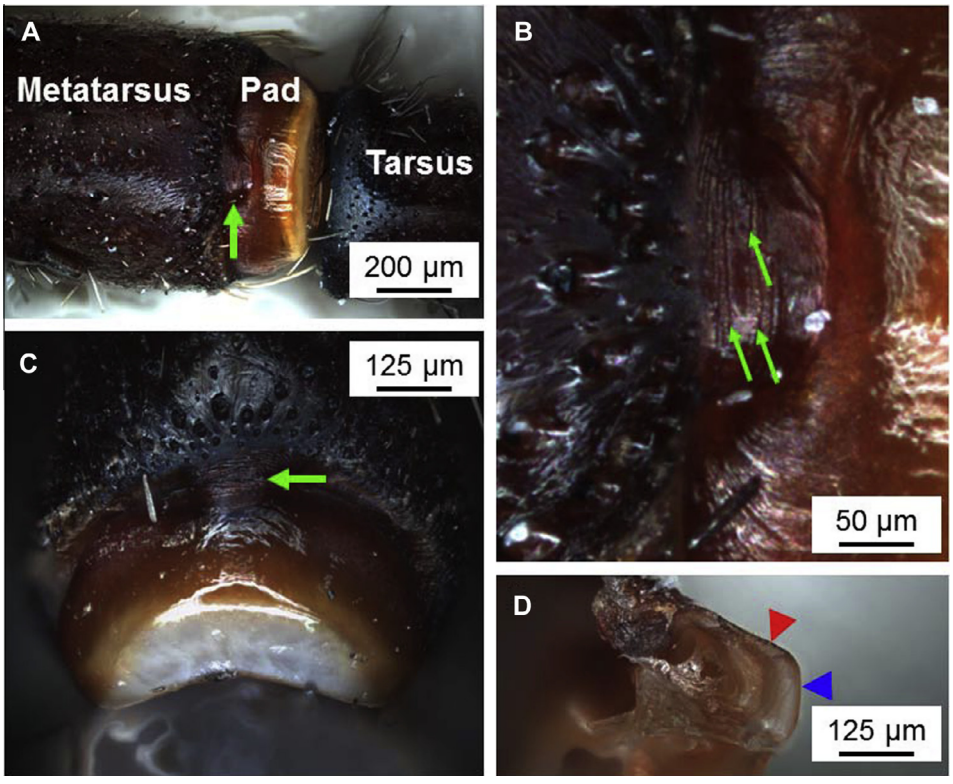

Fig. 2. (A) Optical image of the pad with surrounding hairs removed for a clearer view; the arrow marks the location of the metatarsal lyriform organ. (B) Metatarsal lyriform organ with arrows pointing at several slits. (C) Distal view of the pad (point of contact) looking towards metatarsus. (D) Optical image of a pad sectioned longitudinally with arrowheads marking its "dorsal" (red arrow) and "distal" (blue arrow) surfaces .

Please cite this article in press as: Young SL et al. A spider's biological vibration filter: Micromechanical characteristics of a biomaterial surface. Acta Biomater (2014), http://dx.doi.org/10.1016/j.actbio.2014.07.023

Here, we present new results of our surface force spectroscopic (SFS) study of the viscoelastic nanomechanical properties of the spider pad material by directly measuring the mechanical response of its surface as a function of external temperature and probing rate. Using local mechanical measurements and surface mapping through a range of biologically relevant temperatures (within 15–40 °C) at various frequencies from 0.05 to 20 Hz, we reconstructed a global master-curve for thermomechanical behavior based upon the time–temperature superposition principles at a reference temperature of 19 °C. From this analysis, we obtained relaxation times and demonstrated that peaks of mechanical energy dissipation occur within narrow frequency windows controlled by the surrounding temperature relevant to biological function.

2. Experimental

2.1. Materials

For this study, live adult females of the spider *C. salei* (Ctenidae) were received from the breeding stock of the Department for Neurobiology, University of Vienna (Fig. 1A) [6]. In order to expose the pad for AFM measurements, the hairs surrounding the organ were removed by gently rubbing against the grain with a KimWipe, and by carefully removing the remaining hairs nearest the pad with tweezers. Freshly autotomized legs were also utilized for mechanical measurements, with all experiments taking place within 72 h of the autotomization. In this way, the natural material properties of the spider were not significantly altered due to dehydration, allowing for a close estimate of the temperature-dependent mechanical properties of the pads in live spiders. The mechanical properties of freshly autotomized legs (still hydrated) were identical to those of live spiders. Additionally, the mechanical properties of dehydrated pad material are significantly different (dehydrated pads have an elastic modulus of 200–300 MPa, tested but not presented here, vs. 20 MPa in live spiders).

Pads were sectioned by slicing downward along the dorsal midline of the metatarsus (sagittal section) using a Bard-Parker #10 carbon steel surgical blade. A 1:1 weight mixture of beeswax (Sigma Aldrich) and rosin (colophony, Alfa Aesar) was used to secure individual spider legs and sections onto a glass substrate. A light microscope was employed to confirm that the sectioned surface was oriented parallel to the glass surface to avoid artifacts by scanning at a large angle. The glass substrate was then attached to a custom-made heating bath using silver conductive paste 18DB70X (Electron Microscopy Sciences). The samples were then submerged in high-purity water (18.2 MΩ cm, Synergy UV-R, Millipore) and the chosen temperature set by the user (typically starting at 40 °C and working to lower temperatures). After each temperature adjustment the system was allowed to thermally equilibrate for 30 min such that both the temperature readings and the cantilever deflection were constant. For each individual measurement constant temperature was maintained during the experiment using a thermocouple feedback loop (ILX Lightwave LDT-5948 Precision Temperature Controller) which was attached next to the glass slide. The accuracy of the thermocouple (±0.01 °C) was independently verified using a volume expansion thermometer.

2.2. Atomic force microscopy

AFM was chosen as a technique well suited to measure the micromechanical properties of soft polymeric and biological materials in a non-damaging manner [28–31]. Furthermore, the versatility of AFM facilitates the measurement of surface forces at various temperatures, allowing for the viscoelastic characterization of soft material surfaces [32–36]. All AFM measurements were performed using a Dimension Icon microscope (Bruker) equipped with a Nanoscope V controller. Rectangular n-type Si cantilever probes, with nominal spring constants of 0.2 N m^{-1}, were obtained from MicroMasch (Lady's Island, South Carolina). The radius of curvature at the tip apex was estimated by scanning 20 nm diameter gold nanoparticles and deconvoluting the tip shape (under the standard assumption that the tip apex can be roughly approximated by a parabolic shape) [28]. For the following AFM experiments, a combination of live spider legs and freshly autotomized legs was used to ensure that our experimental results apply to native pad materials of live spiders in their natural environment (Fig. 2). The dorsal and distal surface of the pad were selected for detailed micromechanical probing, as indicated in Fig. 2D.

The cantilever's deflection sensitivity was determined by collecting force–distance curves (FDCs) on a sapphire crystal. The cantilever spring constant, *K*, was measured using the thermal tuning method [28,37]. Topography measurements were made in peak force tapping mode using the established procedure [29], where the AFM tip is moved sinusoidally in the z-direction (normal to the surface which is being measured) and a user-defined force (typically a few nN) is used as a feedback in order to track the surface topography. Scan areas ranged from 500 nm × 500 nm to 20 μm × 20 μm using resolutions of either 512 × 512 or 1024 × 1024 pixels. Scan rates were chosen within 0.5–1 Hz.

The detailed description of the SFS experiments needs a clarification of the terminology. A FDC taken on a sapphire crystal and presented in Fig. 3 illustrates this discussion. In a typical SFS measurement, the user selects a ramp size (the total size of the approach curve), a ramp rate (the inverse of the time it takes to make both the approach and retraction), and a deflection threshold (deflection at which the z-piezo stops extending and begins to retract). In SFS experiments, surface topography causes variations in the point at which the tip first contacts the sample surface. Furthermore, changes in surface stiffness from point to point cause the interaction time between the tip and sample to vary (e.g., a softer sample will deform more, resulting in a longer loading time to reach the deflection threshold). As a result, it is impossible for the AFM to reach the deflection threshold at the exact ramp rate and ramp size as defined by the user under different conditions. To compensate for this, AFM extension and retraction occur over a larger distance than set by the user, but at a velocity which would correspond to the user-defined size-rate pair and unnecessary data

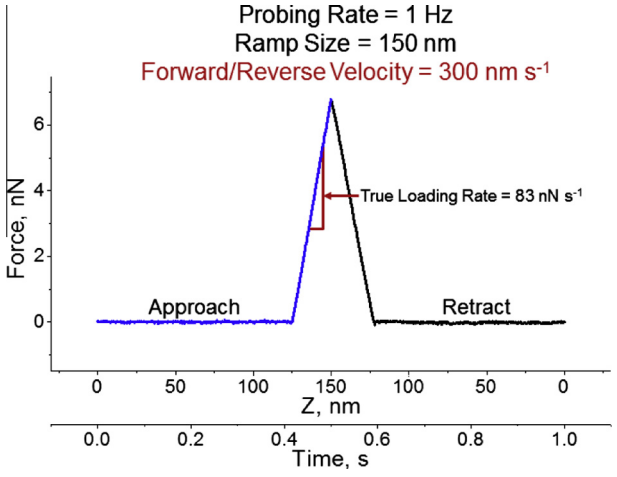

Fig. 3. Sample loading curve taken on a sapphire crystal demonstrating the definition of probing rate, true loading rate and probing velocity.

is truncated. Additional complexity can occur in the leathery regime (between glassy and rubbery behavior) in which the loading curves can become highly non-linear. Therefore, to avoid calculating each individual true loading rate and also the ambiguity of such calculations, which occurs when the true loading rate is non-linear, we group our experiments by "probing rate" (ramp rate).

In order to determine the viscoelastic properties of the pad surfaces, FDCs were taken at 0.05, 0.1, 0.5, 1, 2, 5, 10 and 20 Hz probing rates for each temperature within the range close to what the spiders might see in their natural environment in South America (from 15 °C at night up to 30–40 °C during the day time [6,15]). The manner in which force is applied to the pad by the tarsus is not physically similar to the manner in which the tip is applying forces to the pad surface. To ensure that we work only in the elastic regime, deformation levels were kept below 15 nm and the surface was routinely scanned after making FDCs to check for plastic deformation.

Capillary bridges, which form between the tip and the sample surface, are a common occurrence when scanning in ambient conditions (typically the relative humidity (RH) is ~40%). They produce significantly high snap-to-contact forces, distorting the information provided by the AFM. This distortion can be avoided by keeping the sample and probe completely immersed in water. Therefore, all probing experiments were performed in water. In our case, immersion in water also ensures that the pad material remained fully hydrated (RH > 80% in the spider's natural environment). A saline solution may be more appropriate to immerse our samples to keep the properties as close as possible to the properties of the live spider. However, any exposure to solutions containing charged ions can cause severe corrosion in the electrical components of the scanner and thus should be avoided.

The analysis of the FDCs involved selecting curves from each frequency–temperature set which had low background noise and a clear contact point. Typically, >30 FDCs were collected at different locations and initially analyzed to determine the elastic modulus by fitting with the classical Sneddon equation for the purely elastic deformation of an elastic half space with a rigid paraboloidal punch [31,38,39]:

$$P = \left(\frac{4}{3}\frac{E}{1-\nu^2}R^{1/2}\right)\delta^{3/2} \quad (1)$$

where P is the applied force, R is the radius of curvature of the tip, δ is the penetration depth, ν is Poisson's ratio (chosen to be 0.3 to be consistent with McConney et al. [12]), and E is the elastic modulus of the outermost surface layers. For fitting the FDCs we used unconstrained nonlinear optimization with MatLab software. The error bars presented with the data represent one standard deviation calculated from the elastic modulus fitted from each FDC. The values of modulus calculated for each temperature could then be plotted vs. probing rate. They were shifted accordingly to construct a master curve at 19 °C according to the WLF principle of time–temperature superposition [23].

2.3. Optical microscopy

Optical images were taken under dark-field illumination using a BX-51 microscope with a Dage-MTI XLM high-resolution cooled digital camera at 10× magnification. Because of the highly non-planar nature of our samples and the inherent lack of significant depth of field associated with optical microscopy, the clarity of each optical image was digitally enhanced using the method of focus stacking. Briefly, multiple images (>100) were recorded at different focal planes and the in-focus portions of each image were superimposed. Here we utilized Helicon Focus v. 5.3.14 for the optical image focus-stacking.

2.4. Electron microscopy

Scanning electron microscopy (SEM) images were taken using a JEOL JSM-7500F field emission scanning electron microscope. Fresh pads were extracted from shock-frozen animals, mechanically fractured and mounted on an SEM sample-holder with conductive carbon tape. The measurements were performed in high vacuum (7.5×10^{-8} Torr) in low-magnification mode. The working distance was 11.6 mm at 5.0 kV.

3. Results and discussion

3.1. Surface topography

AFM topographical imaging in high-purity water revealed uniformly distributed pores on the dorsal surface of the pad (Fig. 4). Capping these pores is residual epicuticular fluid, seen as hemispheres with diameters ranging from 500 to 1000 nm. Such a surface porous system can be utilized to deliver surface fluidic layer to serve for lubrication and protection as has been suggested for other species such as snakes [40].

In order to directly measure nanomechanical properties of the pad material, only the surface areas not containing the pores or the epicuticular fluid were examined. The pad material surrounding the pores was very uniform and smooth, with a microroughness of 2-3 nm over an area of 1 μm × 1 μm. This microroughness is higher than previously reported [12] and attributed to the peak force tapping mode in fluid, in which force is applied directly to cause surface deformation. This is in contrast to standard soft tapping in air, in which the amplitude of a vibrating tip is damped by van der Waals forces [28].

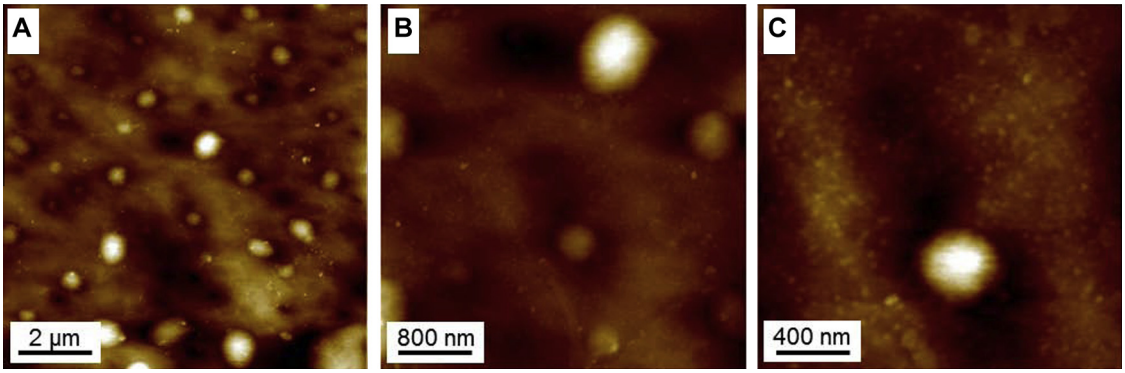

Fig. 4. AFM topography images of the dorsal surface of the metatarsal lyriform organ, showing randomly distributed pore canals. Z-scales: (A) 155 nm, (B) 155 nm, (C) 55 nm.

Please cite this article in press as: Young SL et al. A spider's biological vibration filter: Micromechanical characteristics of a biomaterial surface. Acta Biomater (2014), http://dx.doi.org/10.1016/j.actbio.2014.07.023

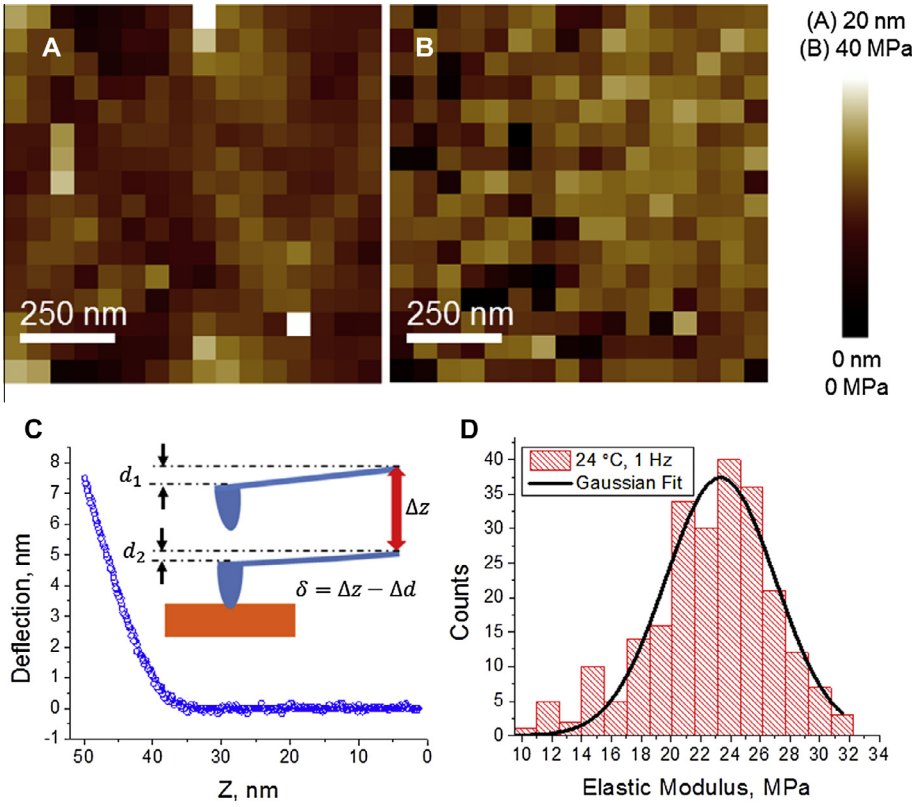

Fig. 5. Topography (A) and modulus (B) maps taken concurrently using SFS on the dorsal surface of the pad. (C) Representative loading curve with an inset schematically showing indentation. (D) Modulus distribution of the pad taken at room temperature. Z-scales: 20 nm (A); 40 MPa (B).

3.2. SFS mapping

The SFS version of AFM allows precise area mapping of tip–sample interactions [28]. SFS entails creating a two-dimensional array of FDCs, which is analyzed to simultaneously map the surface distribution of the elastic modulus and the surface topography (Fig. 5) [28]. 2-D sets of such FDC data are produced by pressing an AFM probe against the sample surface, pixel-by-pixel, across the selected surface area (Fig. 5A, B). Vertical displacement of the probe results in small pad surface deformations. Usually these are within 2–10 nm in the z-direction and are determined by the difference of the z movement of the piezo-element and cantilever deflection (Fig. 5C).

Surface topography was evaluated from AFM images concurrently collected on the dorsal surface of the pad (Fig. 5A). The surface was uniform and thus appropriate for SFS mapping. In the probing studies, in a number of surface areas between 1 and 2 μm^2, 16 × 16 pixel (63–125 nm distance between each pixel) measurement fields were mapped (Fig. 5B). At an average AFM tip radius of only 15–20 nm, each FDC collected in the elastic regime was unique and not affected by the strain fields of subsequent measurements.

After collecting these data sets, the FDCs were analyzed using Sneddon's contact model (Eq. (1)) to produce a map of elastic modulus values calculated under assumption of purely elastic deformation (Fig. 5B) [38,39,41]. Based on the calculated elastic modulus for each pixel (Fig. 5B), the histogram of the surface distribution at a selected temperature and probing frequency was generated (Fig. 5D). The distribution was roughly symmetrical, with a longer low-value tail caused by the topographical distortions (elevated points and the edge of pores). Gaussian approximation of these histograms allowed for the calculation of the average value and standard deviations, as demonstrated in Fig. 5D. In this selected example, calculated for 24 °C and a probing rate of 1 Hz, the average modulus value was 23 ± 4 MPa. This value corresponded very well with the values calculated by McConney et al. [12] for low loading rates at ambient conditions using 5 μm radius borosilicate colloidal probes.

3.3. Viscoelastic response

3.3.1. Glassy-to-rubbery transition

For soft polymeric materials at lower temperatures (in their glassy state) the free volume is limited and large-scale macromolecular motion (segmental motion) is essentially frozen. At higher temperatures, however, the thermal energy in the system provides higher mobility to the polymer macromolecules, allowing for large-scale, reversible segmental chain motion upon the application of a force. This results in a reduced elastic modulus (the rubbery state). The temperature at which a material transitions from the glassy to the rubbery state is the so-called glass transition temperature, T_g [25]. Corresponding changes of mechanical properties around this temperature will be discussed for pad materials in this section.

Fig. 6A presents loading curves taken at 1 Hz probing rate on the dorsal surface of the pad. The dramatic changes in deformational behavior related to the transition from glassy to rubbery behavior can be clearly seen. In general, the slope of the loading curve is a measure of the elastic modulus of the sample. This can be seen from Eq. (1), where the applied force, P, is linearly related to . For low temperatures, e.g., 17 °C, a 9 nm piezo-element motion results in a cantilever deflection of ~7.3 nm, which corresponds to a surface deformation of 1.7 nm (Fig. 6A). At 25 °C, however, a similar tip deflection is only achieved after a z movement of 15 nm that results in an 8 nm surface deformation (Fig. 6A). Such changes

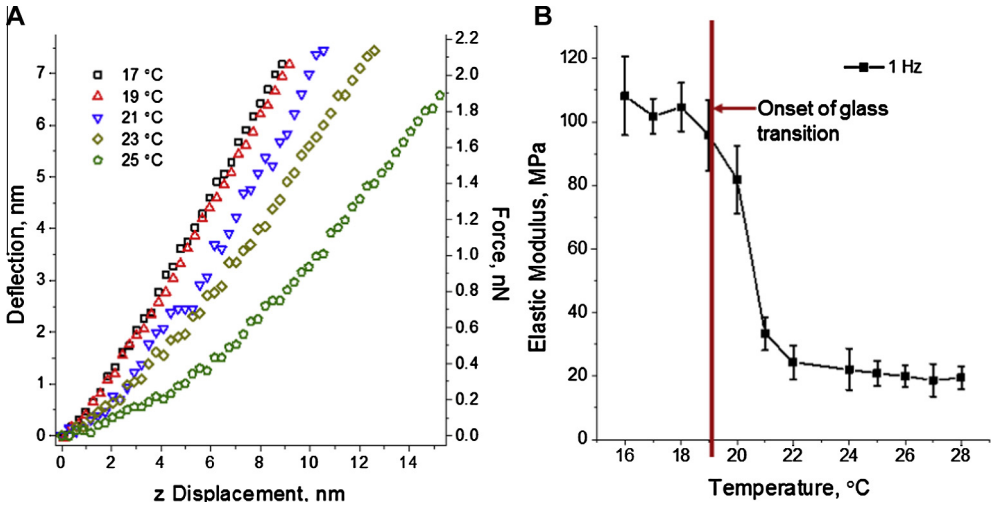

Fig. 6. (A) Representative approach curves taken on the dorsal surface at 1 Hz for the temperatures indicated and showing a change in curve shape and slope through the glass transition temperature range. (B) Elastic modulus vs. temperature of the dorsal surface of the pad using a 1 Hz loading rate.

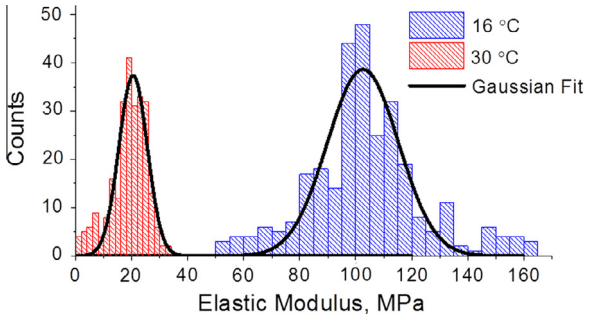

Fig. 7. Elastic modulus distributions of the dorsal surface of the pad at 16 and 30 °C; both distributions were obtained using a 1 Hz probing rate.

imply a change from a high modulus in the glassy state to much more compliant properties in the rubbery state.

Using 1 Hz as a standard probing rate, SFS analysis on the dorsal surface through a range of biologically relevant temperatures at intervals of 1 °C revealed the dependence of the elastic modulus on temperature including the determination of T_g. Elastic moduli were calculated by averaging many (>100) FDCs, which resulted in distributions similar to those shown in Fig. 7 for different temperatures. Fitting with a Gaussian function yielded an average modulus in the glassy regime of 105 ± 11 MPa for measurements taken at 16 °C with a probing rate of 1 Hz. For 30 °C and again using a probing rate of 1 Hz an average modulus of 20 ± 4 MPa was found in the rubbery state (Fig. 6B). According to this data the apparent onset of the glass transition occurs at ~19 °C, with the elastic modulus steeply decreasing above 22 °C. This result is close to that previously reported from colloidal force probing experiments with smaller surface deformations (T_g = 25 ± 2 °C [12]).

3.3.2. Time–temperature analysis

It is worth noting that the experimental probing rate is limited by a number of factors including resonance properties and creep of the piezo-element, the rate at which the detector can collect data, and, at high enough rates, the viscosity of the fluid medium (all measurements were conducted in aqueous environment). Therefore, a complete characterization of the viscoelastic behavior was undertaken by allowing the pad material to thermally equilibrate at each temperature examined between 15 and 40 °C (in this case temperature intervals of 3 and 5 °C were used), and by producing FDCs using probing rates of 0.05, 0.1, 0.5, 1, 2, 5, 10 and 20 Hz at each temperature.

The elastic modulus as a function of probing rate and temperature is further plotted in Fig. 8A. At temperatures sufficiently above or below the glass transition temperature, the rate-dependent behavior of the elastic modulus essentially disappears and its values remain largely constant. At temperatures of 27 °C and higher, the modulus does not change significantly with the probing frequency, with the average modulus of the 32 data points being 18.5 ± 3.9 MPa, which is well in line with the value (~20 MPa) obtained for the single point distribution (30 °C, 1 Hz) presented above. Similarly, at 15 °C, the lowest temperature probed, the modulus does not deviate significantly from ~106 MPa throughout most of the probing rates (Fig. 8A). However, a slight drop-off at 0.05 Hz most likely represents a rate-dependent effect, with some contributions from the greater instability of the measurements at extremely low probing rates with long-time piezo-element creep (generally the standard deviation for 0.1 and 0.05 Hz probing rates was greater than for all other probing rates at all temperatures). Close to room temperature, at 24 °C, a modest upturn in the measured elastic modulus to ~31 MPa is observed for the highest probing rates. However, the most dramatic temperature- and rate-dependent behavior is exhibited in the glassy-to-rubbery transition region at 18–21 °C (Fig. 8A).

We then applied the principle of time–temperature superposition to these probing data, whereby the modulus calculated for a certain apparent probing rate and temperature can be shifted with respect to a reference apparent probing rate and temperature. In this manner, a "universal" time–temperature–modulus relationship was created (as described in detail by Chyasnavichyus et al. [41]). This analysis was accomplished using the WLF equation [23,25]:

$$log\left(\frac{f}{f_0}\right) = \frac{-c_1(T - T_0)}{c_2 + (T - T_0)}, \quad (2)$$

where f is the shifted probing rate, f_0 is the reference probing rate, T is the temperature, T_0 is the reference temperature, and c_1 and c_2 are material-dependent constants. Because no values for these constants are available for the cuticular pad of *Cupiennius*, we used the "universal" polymer constants of $c_1 = 17.44$ and $c_2 = 51.6$ for common amorphous rubbers [12,22,23].

Because the onset of the glass transition was determined to be at ~19 °C (using 1 Hz apparent probing rate and a small temperature

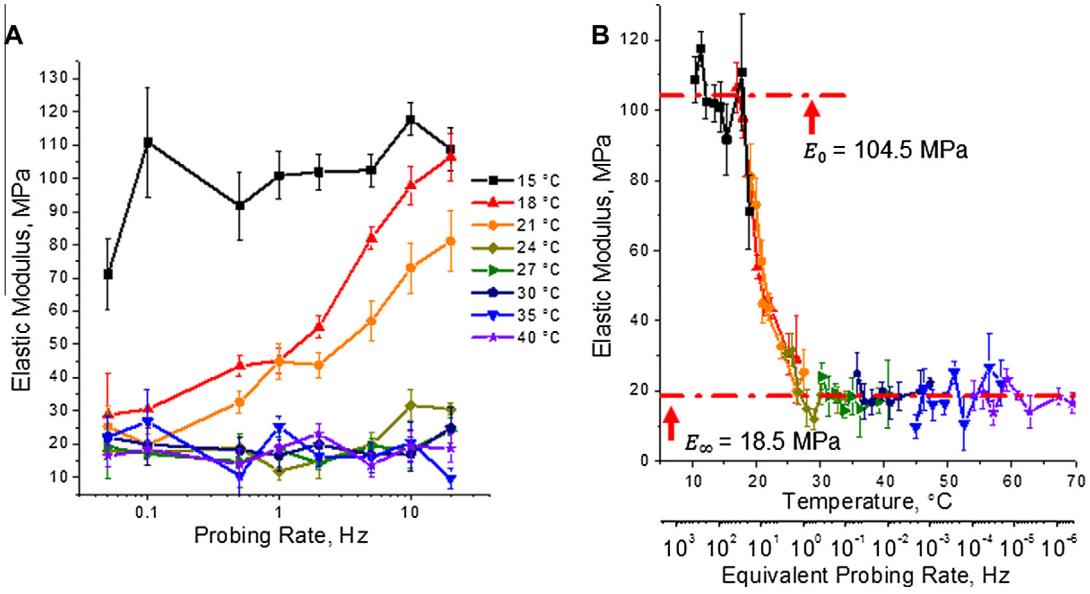

Fig. 8. (A) Elastic modulus vs. probing rate of the dorsal surface of the pad, grouped by measurement temperature. (B) Full time–temperature–modulus relationship of the dorsal surface of the pad obtained using the principle of time–temperature superposition via the WLF equation. Here the top x-axis corresponds to the expected elastic modulus of the pad at a given temperature using a 1 Hz probing rate, while the lower x-axis corresponds to the expected elastic modulus of the pad at a given probing frequency at a measurement temperature of 19 °C. The upper and lower bounds are averages taken from the extreme data points (i.e., the lowest temperatures and highest probing rates, and the highest temperatures and lowest probing rates).

interval), this was chosen as the reference temperature (T_0). A universal time–modulus relationship was then obtained by solving Eq. (2) for f, using the experimental probing rates as f_0. Similarly, the temperature–modulus relationship was then determined by using the calculated f values, choosing f_0 equal to 1 Hz, and solving Eq. (2) for the equivalent temperatures, T (here T_0 was the experimental measurement temperatures). In this way the viscoelastic mechanical behavior of the pad material could be estimated for a much wider range of temperatures and probing rates (Fig. 8B). The resultant "master" curve for the elastic modulus of the dorsal surface of the pad displays the full time–temperature–elastic modulus relationship with two different variables. Here, the onset of the glassy-to-rubbery transition occurs at 18 °C, where the elastic modulus decreases sharply from an average of 105 to 19 MPa at 26 °C. Similarly, when using the lower x-axis one can observe that at 19 °C, a temperature the pad surface is likely to experience in its natural environment [1], a sharp increase in elastic modulus occurs at ~1 Hz probing rate. From these results one can estimate how the pad should respond under a given temperature or probing rate. It should be noted that the present measurements were made at temperatures between 15 and 40 °C and projected to a wider range using the WLF equation. However, temperatures >40 °C will hardly ever be experienced by *Cupiennius* and further decreases in the modulus of the pad may occur at such elevated temperatures.

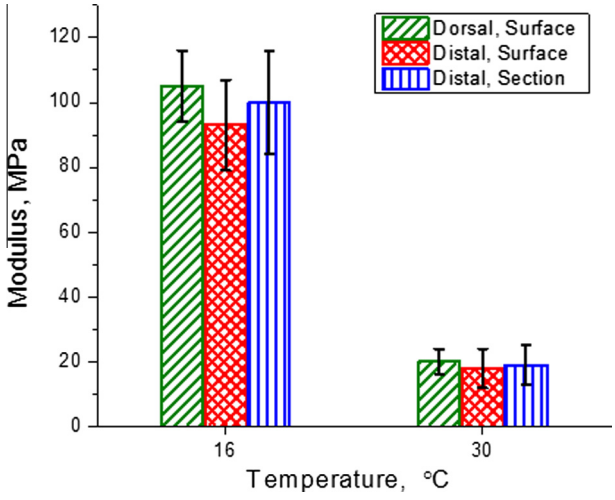

Fig. 9. Summarized elastic modulus values for different locations of the pad measured below and above T_g.

3.4. Mechanical properties of the distal surface of the pad

The distal surface of the pad serves as the contact point with the tarsus (Fig. 2). Therefore, its mechanical properties are particularly important. In order to examine this area, a freshly autotomized leg was clamped such that the pad's distal surface was facing upwards and reachable by the AFM tip. The tarsus was then deflected downwards and secured using a small amount of beeswax/rosin mixture. SFS of the distal surface was then performed using a probing rate of 1 Hz at two extreme temperatures, 16 and 30 °C (Fig. 9). The analysis of each data set gave similar modulus distributions, with an average value of 93 ± 14 MPa at 16 °C and 18 ± 6 MPa at 30 °C. From this comparison we concluded that the viscoelastic mechanical properties of the distal and dorsal surfaces of the pad are the same. Since time and temperature are interrelated in viscoelastic systems, the elastic modulus at low/high temperatures at a given frequency correspond to the elastic modulus measured with high/low strain rates. Thus, the mechanical contact with the tarsus results in a higher effective modulus at high frequencies than at low frequencies. This implies a more effective mechanical energy transmission to the sensory slits, and hence high-pass filtering properties, as has been suggested earlier [6,12].

Arthropod cuticle is a complex hierarchical, multilayered material with a wide range of properties serving a multitude of functions [42–46]. Specifically, the exoskeleton of *C. salei* contains a stiff exocuticle that is a laminated structure composed of sheets of parallel chitin fibrils embedded in a protein matrix which are rotated between each successive layer [43,47,48]. This exocuticle

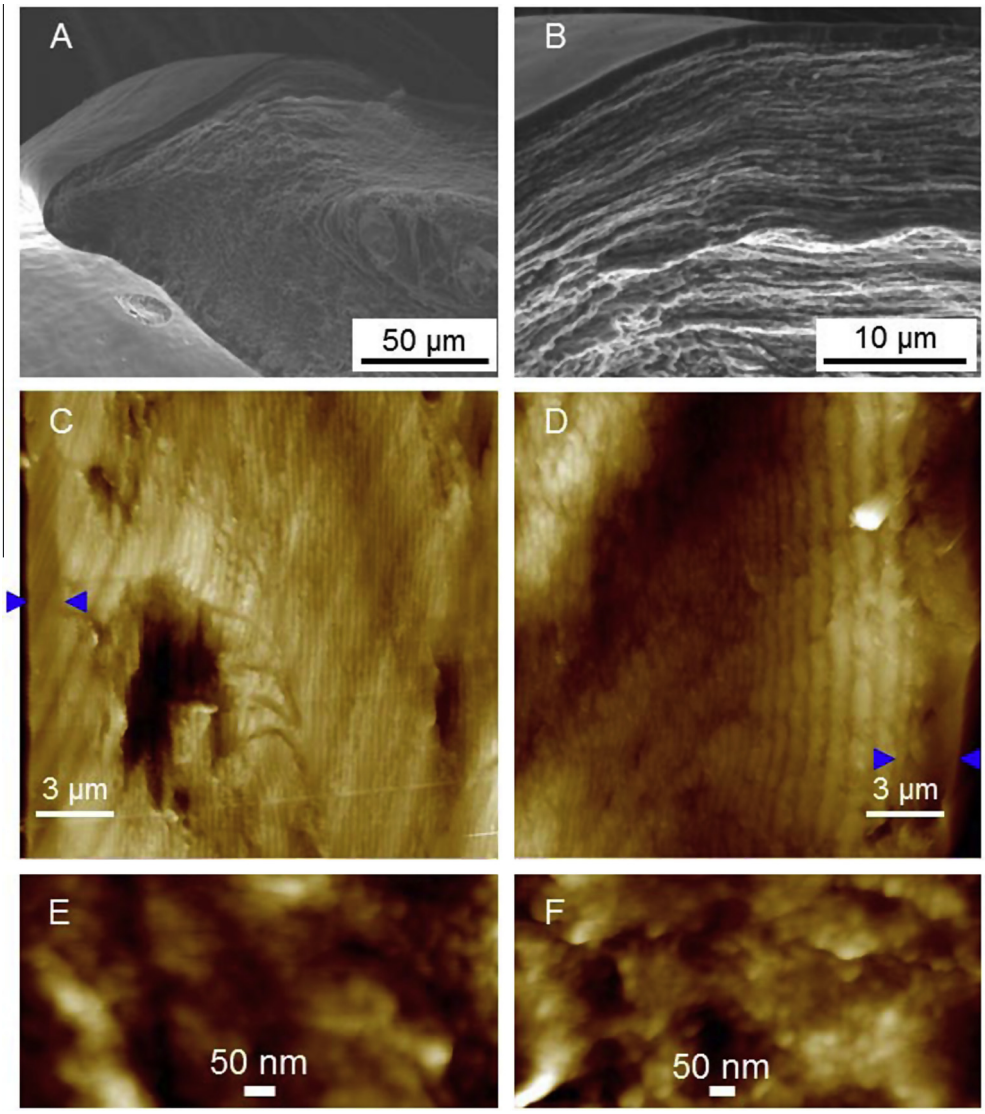

Fig. 10. (A, B) SEM images of the pad showing a uniform coverage of an ~1–2 μm thick outer layer. AFM topography images of the pad section at the dorsal surface (C) and distal surface (D); blue arrows mark the outer layer. High-resolution height images taken on the longitudinal section of the coating at the dorsal (E) and distal (F) locations. Z-scales: (C) 240 nm, (D) 120 nm, (E) 20 nm, (F) 20 nm.

is covered by the outermost layer of the exoskeleton, the epicuticle. The composition of this layer is not characterized as well as other layers that comprise the exoskeleton of *Cupiennius*. It is thought to be made up of proteins and lipids which are not highly oriented like the chitin fibrils in the adjacent exocuticle. According to measurements on *C. salei* [6,49], the thickness of the epicuticle on the metatarsal joint of the leg typically is <100 nm.

In order to test whether the pad's mechanical properties measured here are characteristic of the topmost surface layer of the pads or are also affected by the supporting microstructure, we analyzed saggital sections of the pad and confirmed its layered morphology as suggested previously for the exocuticle of *Cupiennius* (Fig. 10) [43,47]. An outermost epicuticular region covers the entire pad. Its thickness of 1–2 μm is nearly an order of magnitude larger than that previously measured on the metatarsal joint [6,49]. AFM topographical measurements confirm the epicuticle's unusual thickness (Fig. 10C, D). According to high-resolution images of the sections (Fig. 10E, F) the epicuticle shows a globular texture and, as expected from previous studies, lacks a chitin-based laminated morphology. The thickness of the pad's epicuticle greatly reduces any contribution from the underlying substructure to the elastic modulus calculated from AFM probing. The detailed analysis of subsurface morphologies and their role in overall mechanical behavior will be discussed elsewhere.

3.5. Relationship to natural stimuli

In the SFS measurements described above, the force was applied in a linear manner. However, in nature vibratory stimuli are transmitted to *Cupiennius* as a complex mixture of superimposed sinusoids of varying frequencies [6,9]. Therefore, it is important to relate the data we have obtained here to the expected response of the pad material to sinusoidal loading, which also allows for a direct comparison with the electrophysiologically determined threshold curves [9]. In order to do so, we first analyzed the time–temperature variation of SFS data to determine the relaxation times of the pad material.

3.5.1. Relaxation times of pad surfaces

Viscoelastic systems are usually modeled as an idealized combination of spring and dashpot elements in terms of Voight or Maxwell models [21,22,39]. Because the deformation levels throughout our measurements remained too low to cause plastic deformation, the pad was modeled using a standard linearly viscoelastic solid

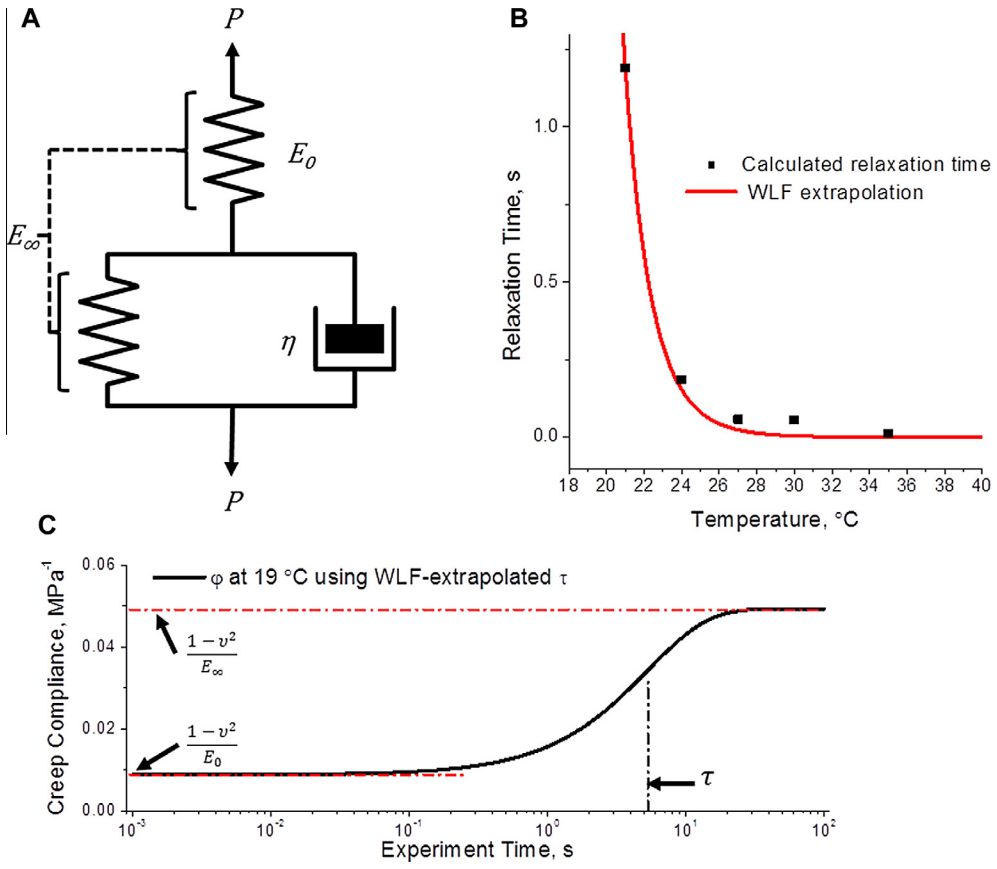

Fig. 11. (A) Idealized spring and dashpot model of the standard linearly viscoelastic solid. (B) WLF fit for the relaxation time at the reference temperature of 19 °C (inset), and the extrapolation of all relaxation times for the entire temperature range measured. (C) Creep compliance function for the pad at 19 °C showing the location of the relaxation time along the curve and the upper and lower limits, which were determined experimentally.

(SLS model) in order to simulate its complete time–temperature biomaterial properties (Fig. 11A). The application of load P to the linear viscoelastic solid results in an instantaneous elastic response characterized by a spring with an effective modulus E_0 (instantaneous modulus). At sufficiently long measurement time, the dashpot element relaxes and the material has an elastic response equivalent to two springs in series, which corresponds to the so-called infinite elastic modulus E_∞. This effect is known as "delayed elasticity" and can be characterized by the creep compliance function [39,41]:

$$\varphi(t) = \frac{1-\upsilon^2}{E_\infty}\left(1-\left(1-\frac{E_\infty}{E_0}\right)e^{-t/\tau}\right) \quad (3)$$

where τ is the relaxation time of the material, which is a function of the dashpot's dynamic viscosity, η, and can be used to quantify the timescale of large-scale molecular motion at a given temperature, and t is a point in time after the application of load P. When the creep compliance function is plotted against $log(t)$, $log(\tau)$ represents the point of inflection of the sigmoidal curve (Fig. 11C) [21].

The temperature- and probing rate-dependent behavior observed on the pad surface (and viscoelastic materials in general) occurs when the thermal energy added to the system is sufficient to cause the rate for large-scale macromolecular rearrangements to be close to the timescale of the load application. In the glassy-to-rubbery transition regime, the stress–strain relationship deviates from the classical Hookean behavior (spring-on-spring), due to the presence of the viscous dashpot, and the linear relationship between $\delta^{3/2}$ and the applied force, P, is replaced by a time-dependent function [39,41]. Chyasnavichyus et al. [41] have recently shown that the time-dependent penetration function suggested by Johnson [39] can be employed to determine τ as a function of temperature:

$$\delta^{3/2}(t) = \frac{3UL}{4\sqrt{R}}\frac{1-\upsilon^2}{E_\infty}\left(\frac{t}{\tau}-\left(1-\frac{E_\infty}{E_0}\right)(1-e^{-t/\tau})\right) \quad (4)$$

where U is the loading rate (assumed to be constant), and L is the total time the tip is in contact with the surface during the approach fraction of the FDC. Here, we take the average of the extreme values of the calculated modulus shown in Fig. 8 to be E_∞ and E_0 (18.5 and 104.5 MPa, respectively). Next, $\delta^{3/2}$ vs. time curves were fitted according to Eq. (4) to determine τ at 35, 30, 27, 24 and 21 °C (Fig. 11B). At the highest temperatures, the relaxation time of the pad material is short, ranging from 0.013 to 0.055 s. At 21 °C relaxation times are increased dramatically, up to 1.20 s, suggesting very slow relaxation at this temperature range as is characteristic of highly viscous materials [21,41].

Further fitting at lower temperatures is limited due to substantial errors resulting from a relaxation time exponentially increasing with temperature and becoming much longer than the actual contact portion of any FDC that we can produce with the AFM [41]. However, lower values of τ can be extrapolated using the WLF theory by fitting the previously determined relaxation times for τ_0 with:

$$\tau = \tau_0 10^{\frac{-c_1(T-T_0)}{c_2+T-T_0}}, \quad (5)$$

where τ_0 is the relaxation time at the reference temperature, T_0 (19 °C) (solid line in Fig. 11B). From this analysis, it was determined that the relaxation time should increase to 5.4 s for the pad surface at 19 °C, and further increase to as much as 156 s at 15 °C. Thus the pad material is made more resistive (i.e., the dashpot element

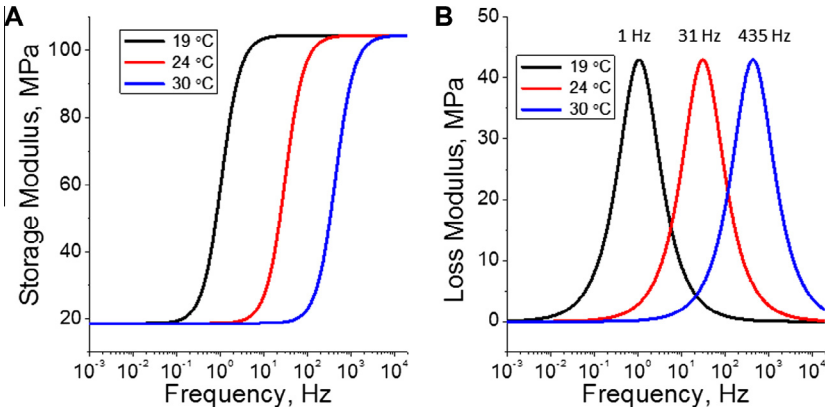

Fig. 12. Storage (A) and loss (B) moduli calculated using Eqs. (5) and (6) demonstrating the dependence of the mechanical properties on the loading frequency (force applied sinusoidally) at 19, 24 and 30 °C.

becomes infinitely viscous) to mechanical deformation at low temperatures, increasing the effectiveness of stimuli transmission to the HS-10 organ (Fig. 11B).

3.5.2. Loss and storage moduli

A viscoelastic material's mechanical response to a sinusoidally applied stress is described by its storage and loss moduli, E′ and E″, respectively [21,22]. During the application of periodic forces, the storage modulus represents the elastic response for which the deformation of the material is in phase with the force. Conversely, the loss modulus is the out-of-phase, viscous response where mechanical energy is dissipated. E′ and E″ can be related to the relaxation time and the previously calculated values of E_0 and E_∞ by [41,50]:

$$E' = E_\infty \frac{1+\omega^2\tau^2(E_\infty/E_0)}{1+\omega^2\tau^2(E_\infty/E_0)^2}, \quad (6)$$

$$E'' = E_\infty \frac{\omega\tau(1-(E_\infty/E_0))}{1+\omega^2\tau^2(E_\infty/E_0)^2}, \quad (7)$$

where ω is the frequency of the sinusoidal force.

E′ and E″ are plotted in Fig. 12 for relaxation times corresponding to 19, 24 and 30 °C. From this, one can see that increases in temperature shift the rubbery-to-glassy transition and the peak of E" to higher frequencies. Examining the behavior of E′ and E″ at 24 °C allows us to compare with the tuning (threshold) curves produced at room temperature by Barth and Geethabali [9]. Here E′ increases rapidly from 24 to 99 MPa between 8 and 115 Hz, with maximum energy dissipation (maximum E″) occurring at 31 Hz, which is very close to the value of ~40 Hz beyond which the spider becomes highly sensitive to substrate vibrations [6,9]. On the other hand, at 30 °C E′ only begins increasing after 116 Hz, while the maximum of E″ occurs at 435 Hz. Therefore mechanical energy applied at frequencies <435 Hz at 30 °C is dissipated and not as easily transferred through the pad to the slits. At 19 °C the maximum energy dissipation occurs at 1 Hz, and E′ quickly reaches its maximum (104.5 MPa) after ~10 Hz. This implies that at 19 °C the spider is highly sensitive to substrate vibrations with frequencies >5–10 Hz.

4. Conclusions

We have shown here a non-destructive probing method can be applied to a natural biomaterial, allowing for a complete viscoelastic characterization of the pad surface materials not possible by any other means. Utilizing the standard linear viscoelastic solid model, we were able to describe the universal time–temperature-dependent mechanical behavior. By applying this approach, the dependence of the elastic modulus of the metatarsal pad of *C. salei* on both temperature and probing rate could be revealed. The onset of the glassy-to-rubbery transition occurs at 19 °C, slightly below regular room temperature. In a narrow range from 18 to 24 °C the pad material exhibited highly time- and temperature-dependent mechanical behavior, with nominal elastic modulus values dropping from 105 MPa at the lowest temperatures to 19 MPa at the highest temperatures studied here. In contrast, the relaxation times increased dramatically at lowered temperatures from tens of milliseconds to seconds below 20 °C, thus making the pad surface a highly damping viscous material at intermediate temperatures with maximum dissipation of mechanical energy. This range likely represents temperatures in which *Cupiennius* spends most of its active hours (i.e., night time, when the mountainous area in which it is found cools to ~20 °C) [15]. In the range where the pad is the most rate- and temperature-dependent, the relaxation time values ranged from ~0.1 to 1 s. Such viscoelastic properties undoubtedly contribute to the high-pass behavior of the HS-10 organ and to the spider's sensitivity to high-frequency signals. Low-frequency signals typical of environmental noise [6,9,20] are filtered out by the epicuticle and require larger tarsal deflections to elicit a neural response [9].

The distal surface of the pad was directly measured here in comparison to the dorsal surface for the first time. Both showed similar mechanical properties. More research into the mechanical properties of all structures involved is needed to determine how substrate vibrations are transmitted to the slits proper of the spider's vibration receptor. Their physiological high-pass characteristics to a large extent can now be explained by the viscoelastic mechanical properties of epicuticle. It should be borne in mind, however, that the metatarsal organ will respond to low-frequency stimuli as well, provided these are strong enough. Under these circumstances in particular, which may also occur during locomotion, rapid escape and complex movements such as those involved in spinning the egg-sac or turning around in small crevices, the complex overall structure and substructure of the pad may not only allow effective stimulus transmission at low frequency but also help to provide mechanical robustness and avoid damage. In addition, the mechanical properties of the overall structure (and substructure) of the pad might affect the transmittance and transformation of vibratory stimuli and be used to concentrate strains onto the metatarsal organ, as suggested earlier [6].

Acknowledgements

Financial support was received from the National Science Foundation, Division of Materials Research under World Materials

Network Award DMR-1209332 and DMR-1002810 as well as the GT Microanalysis Center. We are grateful to the Department for Neurobiology, University of Vienna for providing the spiders.

Appendix A. Figures with essential color discrimination

Certain figures in this article, particularly Figs. 1–12 are difficult to interpret in black and white. The full color images can be found in the on-line version, at http://dx.doi.org/10.1016/j.actbio.2014.06.035.

References

[1] Gorb S. Attachment devices of insect cuticle. Dordrecht: Kluwer; 2001.
[2] Bar-Cohen Y, editor. Biomimetics: biologically inspired technologies. Boca Raton, FL: CRC/Taylor & Francis; 2006.
[3] Terashima S, Goris RC, editors. Infrared receptors and the trigeminal sensory system. Amsterdam: Harwood Academic; 1999.
[4] Peleshanko S, Julian MD, Ornatska M, McConney ME, LeMieux MC, Chen N, et al. Hydrogel-encapsulated microfabricated haircells mimicking fish cupula neuromast. Adv Mater 2007;19:2903–9.
[5] Netten S. Hydrodynamic detection by cupulae in a lateral line canal: functional relations between physics and physiology. Biol Cyber 2006;94:67–85.
[6] Barth FG. A spider's world: senses and behavior. Heidelberg: Springer-Verlag; 2002.
[7] Sane SP, McHenry MJ. The biomechanics of sensory organs. Integr Comp Biol 2009;49:i8–i23.
[8] Barth FG. Sensory perception: adaptation to lifestyle and habitat. In: Barth F, Giampieri-Deutsch P, Klein H-D, editors. Sensory perception. Vienna: Springer-Verlag; 2012. p. 89–107.
[9] Barth FG, Geethabali. Spider vibration receptors: threshold curves of individual slits in the metatarsal lyriform organ. J Comp Physiol 1982;148:175–85.
[10] Barth FG, Bleckmann H, Bohnenberger J, Seyfarth E-A. Spiders of the genus Cupiennius Simon 1891 (Araneae, Ctenidae). II. On the vibrational environment of a wandering spider. Oecologia 1988;77:194–201.
[11] Barth FG. How to catch the wind: spider hairs specialized for sensing the movement of air. Naturwissenschaften 2000;87:51–8.
[12] McConney ME, Schaber CF, Julian MD, Barth FG, Tsukruk VV. Viscoelastic nanoscale properties of cuticle contribute to the high-pass properties of spider vibration receptor (*Cupiennius salei* Keys). J R Soc Interface 2007;4:1135–43.
[13] McConney ME, Schaber CF, Julian MD, Eberhardt WC, Humphrey JAC, Barth FG, et al. Surface force spectroscopic point load measurements and viscoelastic modelling of the micromechanical properties of air flow sensitive hairs of a spider (*Cupiennius salei*). J R Soc Interface 2009;6:681–94.
[14] Klopsch C, Kuhlmann HC, Barth FG. Airflow elicits a spider's jump towards airborne prey. I. Airflow around a flying blowfly. J R Soc Interface 2012;9:2591–602.
[15] Barth FG, Seyfarth EA. *Cupiennius salei* Keys (Araneae) in the highlands of Central Guatemala. J Arachnol 1979;7:255–63.
[16] Barth FG. Vibratory communication in spiders: adaptation and compromise at many levels. In: Lehrer M, editor. Orientation and Communication in Arthropods. Basel: Birkhäuser; 1997. p. 247–72.
[17] Barth FG, Libera W. Ein Atlas der Spaltsinnesorgane von *Cupiennius salei* Keys. Chelicerata (Araneae). Z Morph Tiere 1970;68:343–69.
[18] Barth FG. Arthropod strain sensors. In: Bhushan B, editor. Encycl Nanotechnol. Berlin: Springer-Verlag; 2012. p. 127–36.
[19] Schaber CF, Gorb SN, Barth FG. Force transformation in spider strain sensors: white light interferometry. J R Soc Interface 2012;9:1254–64.
[20] Barth FG. Spider strain detection. In: Barth FG, Humphrey JAC, Srinivasan MV, editors. Front Sens. Vienna: Springer-Verlag; 2012. p. 251–73.
[21] Roylance, D. Engineering Viscoelasticity, October 2001. [online resource, accessed 11 November 2013] url: <http://web.mit.edu/course/3/3.11/www/modules/visco.pdf>.
[22] Krevelen DWv. Properties of polymers: their correlation with chemical structure, their numerical estimation and prediction from additive group contributions. 3rd completely rev. ed. Amsterdam: Elsevier; 1990.
[23] Williams ML, Landel RF, Ferry JD. The temperature dependence of relaxation mechanisms in amorphous polymers and other glass-forming liquids. J Am Chem Soc 1955;77:3701–7.
[24] Tobolsky AV. Stress relaxation studies of the viscoelastic properties of polymers. J Appl Phys 1956;27:673–85.
[25] Sperling LH. Introduction to physical polymer science. 4th ed. Hoboken, NJ: Wiley; 2006.
[26] Barth FG, Humphrey JAC, Secomb TW. Sensors and sensing in biology and engineering. Vienna: Springer-Verlag; 2003.
[27] Fratzl P, Barth FG. Biomaterial systems for mechanosensing and actuation. Nature 2009;462:442–8.
[28] Tsukruk VV, Singamaneni SS. Scanning probe microscopy of soft matter: fundamentals and practices. Weinheim: Wiley-VCH; 2011.
[29] Chizhik SA, Huang Z, Gorbunov VV, Myshkin NK, Tsukruk VV. Micromechanical properties of elastic polymeric materials as probed by scanning force microscopy. Langmuir 1998;14:2606–9.
[30] Young SL, Gupta M, Hanske C, Fery A, Scheibel T, Tsukruk VV. Utilizing conformational changes for patterning thin films of recombinant spider silk proteins. Biomacromolecules 2012;13:3189–99.
[31] Butt H-J, Cappella B, Kappl M. Force measurements with the atomic force microscope: technique, interpretation and applications. Surf Sci Rep 2005;59:1–152.
[32] Cappella B, Kaliappan SK, Sturm H. Using AFM force–distance curves to study the glass-to-rubber transition of amorphous polymers and their elastic–plastic properties as a function of temperature. Macromolecules 2005;38:1874–81.
[33] Cappella B, Kaliappan SK. Determination of thermomechanical properties of a model polymer blend. Macromolecules 2006;39:9243–52.
[34] Tsui OKC, Wang XP, Ho JYL, Ng TK, Xiao X. Studying surface glass-to-rubber transition using atomic force microscopic adhesion measurements. Macromolecules 2000;33:4198–204.
[35] Tsukruk VV, Gorbunov VV, Huang Z, Chizhik SA. Dynamic microprobing of viscoelastic polymer properties. Polym Int 2000;49:441–4.
[36] McConney ME, Singamaneni S, Tsukruk VV. Probing soft matter with the atomic force microscopies: imaging and force spectroscopy. Polym Rev 2010;50:235–86.
[37] Cook S, Schaffer TE, Chynoweth KM, Wigton M, Simmonds RW, Lang KM. Practical implementation of dynamic methods for measuring atomic force microscope cantilever spring constants. Nanotechnology 2006;17:2135–45.
[38] Sneddon IN. The relation between load and penetration in the axisymmetric Boussinesq problem for a punch of arbitrary profile. Int J Eng Sci 1965;3:47–57.
[39] Johnson KL. Contact mechanics. Cambridge: Cambridge University Press; 1985.
[40] Hazel J, Stone M, Grace MS, Tsukruk VV. Nanoscale design of snake skin for reptation locomotions via friction anisotropy. J. Biomech 1999;32:477–86.
[41] Chyasnavichyus M, Young SL, Tsukruk VV. Probing of polymer surfaces in the viscoelastic regime. Langmuir 2014. http://dx.doi.org/10.1021/la404925h.
[42] Bouligand Y. Theory of microtomy artefacts in arthropod cuticle. Tissue Cell 1986;18:621–43.
[43] Barth FG. Microfiber reinforcement of an arthropod cuticle—laminated composite-material in biology. Z Zellforsch mikrosk Anat 1973;144:409–33.
[44] Politi Y, Priewasser M, Pippel E, Zaslansky P, Hartmann J, Siegel S, et al. A spider's fang: how to design an injection needle using chitin-based composite material. Adv Funct Mater 2012;22:2519–28.
[45] McConney ME, Anderson KD, Brott LL, Naik RR, Tsukruk VV. Bioinspired material approaches to sensing. Adv Funct Mater 2009;19:2527–44.
[46] Erko M, Hartmann MA, Zlotnikov I, Valverde Serrano C, Fratzl P, Politi Y. Structural and mechanical properties of the arthropod cuticle: comparison between the fang of the spider *Cupiennius salei* and the carapace of American lobster *Homarus americanus*. J Struct Biol 2013;183:172–9.
[47] Neville A. Biology of fibrous composites: development beyond the cell membrane. New York: Cambridge University Press; 1993.
[48] Bouligand Y. Twisted fibrous arrangements in biological materials and cholesteric mesophases. Tissue Cell 1972;4:189–217.
[49] Barth FG. Die Feinstruktur des Spinnenintegu ments. Z Zellforsch Mikrosk Anat 1969;97:137–59.
[50] Emri I, Tschoegl N. Generating line spectra from experimental responses. Rheol Acta 1997;36:303–6.